Supersonic Retropropulsion Experimental Results from the NASA Ames 9- x 7-Foot Supersonic Wind Tunnel

Scott A. Berry[1], **Matthew N. Rhode**[2], **and Karl T. Edquist**[3]
NASA Langley Research Center, Hampton, VA 23681

Supersonic retropropulsion was experimentally examined in the Ames Research Center 9x7-Foot Supersonic Wind Tunnel at Mach 1.8 and 2.4. The experimental model, previously designed for and tested in the Langley Research Center Unitary Plan Wind Tunnel at Mach 2.4, 3.5 and 4.6, was a 5-in diameter 70-deg sphere-cone forebody with a 9.55-in long cylindrical aftbody. The forebody was designed to accommodate up to four 4:1 area ratio nozzles, one on the model centerline and the other three on the half radius spaced 120-deg apart. Surface pressure and flow visualization were the primary measurements, including high-speed data to investigate the dynamics of the interactions between the bow and nozzle shocks. Three blowing configurations were tested with thrust coefficients up to 10 and angles of attack up to 20-deg. Preliminary results and observations from the test are provided.

Nomenclature

M	= Mach number	α	= angle of attack, deg
Re	= Reynolds number	β	= angle of sideslip, deg
C_p	= pressure coefficient	A_{Ref}	= area reference, in^2
T	= temperature, deg-F or deg-R	ϕ	= model roll, deg
P	= pressure, psia or psf	r, θ	= model polar coordinates
q	= dynamic pressure, psf		
C_T	= thrust coefficient, = $T^*/q_\infty A_{Ref}$	*Subscripts:*	
T^*	= thrust, lbf	T	= stagnation or total conditions
x, y, z	= model coordinate system, in	∞	= freestream conditions
X, Y, Z	= tunnel coordinate system, in	j	= jet conditions

I. Introduction

Entry, descent, and landing (EDL) is a critical component of all planetary surface-exploration programs and is essential for mission success. Each mission typically provides unique design requirements and systems engineering challenges that should be addressed many years ahead of EDL architecture development. Thus, for successful application to future missions, EDL technologies require continuous investment by those interested in space exploration. With many recent successful Mars robotic landings one might infer that EDL is a mature technology. Indeed, with EDL system architectures derived from the Viking-era development effort, all with a 70-deg sphere-cone aeroshell, an ablative thermal protection system, and supersonic parachutes, these missions were fortunate to have similar design requirements. However, with payload size and weight growing with each successive mission, the limits of the Viking-era approach to EDL are presently being tested.[1] In particular, these robotic Mars missions have utilized parachutes for a significant portion of the terminal deceleration required to safely land less than a metric ton on the surface. This approach cannot be scaled up to larger payloads due to physical limits imposed by parachute size and materials. For a manned mission to Mars, landed masses on the order of tens of metric tons are required. A proposed alternative to parachutes is to use propulsive deceleration early in the trajectory, during supersonic flight, instead of just at the terminal-landing phase. Thus, supersonic retropropulsion (SRP), or the use of engine thrust directed into the oncoming supersonic freestream flow, is deemed

[1] Aerospace Engineer, Aerothermodynamics Branch, m/s 408a, AIAA Associate Fellow.
[2] Aerospace Engineer, Aerothermodynamics Branch, m/s 408a, AIAA Senior Member.
[3] Aerospace Engineer, Atmospheric Flight & Entry Systems Branch, MS 489, AIAA Senior Member.

an enabling technology for future large payload missions to Mars. SRP was one of the focus areas of the EDL project in the Exploration Technology Development and Demonstration program. For further discussions of SRP from a systems analysis and performance perspective, see Refs. 2 - 5. A broader SRP-related literature survey is provided in Refs. 6 and 7.

To date, only a handful of studies have been conducted to understand the fluid dynamic phenomena associated with SRP; most of those studies were performed decades ago, for example see Ref. 8. Typically, these older studies were exploratory in nature, designed to investigate the aerodynamic behavior of various Viking-era configurations. While useful for providing key insights into the complex interaction between a supersonic freestream and an opposing rocket plume, the historical reports do not contain enough detail for comparison against modern computational fluid dynamics (CFD) codes.[9] For instance, while static force and moment response characteristics are often reported, the interaction dynamics are not discussed, nor captured in the still images and time averaged data. Figure 1 provides a two-dimensional sketch of a complex three-dimensional flowfield for a single nozzle with the jet plume forcing the bow shock away from the body. Under high thrust conditions, the supersonic plume is in turn compressed into a broad barrel shock with a Mach termination disk that forms as the plume flow decelerates. An annular "triple point" is formed at the corner between the barrel shock and Mach disk. A "free" or virtual stagnation point is situated somewhere between the opposing flows represented by the bow and barrel shocks. At the base of the plume, an annular recirculation zone develops. The fluidic nature of this complex interaction and recirculation is likely to be unsteady, but to what degree and for which conditions are not well understood. Thus, a modern SRP experiment, one specifically designed for CFD validation[10], is intended to allow for higher fidelity comparisons. From a computational perspective, SRP represents a challenging problem for use as a test case for assessing CFD modeling strengths and weaknesses.

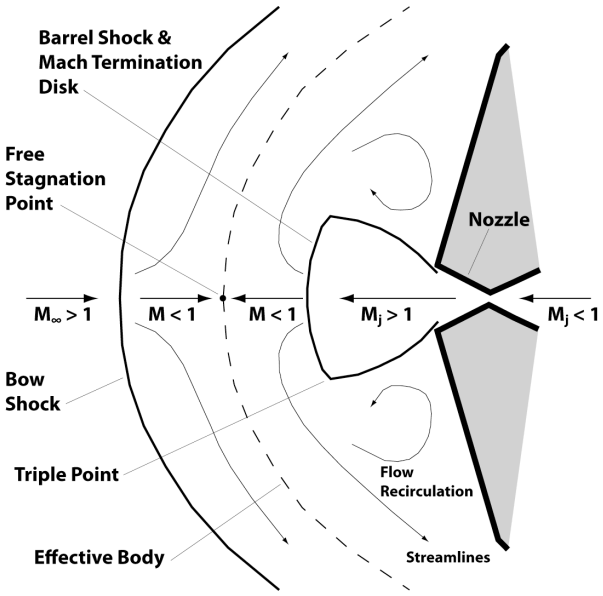

Figure 1 – Conceptual sketch of SRP flow features

The present paper discusses trends and observations obtained from a recent experimental SRP study in the Ames Research Center (ARC) 9- x 7-Foot Supersonic Wind Tunnel (SWT). Reference 11 provides similar results obtained from an earlier test in the Langley Research Center Unitary Plan Wind Tunnel, while Ref. 12 reviewed the philosophy and approach utilized in designing the model and run matrix. The larger test section of the 9x7 SWT allowed for blockage-free testing at lower Mach numbers and/or at higher thrust values. While this study was intended as a validation experiment in support of improved CFD models and capabilities, the present paper will strictly focus on a review of the SRP experimental results. A myriad of papers have recently been published that provide detailed post-test CFD comparisons to the experimental results, for instance see Refs. 13-18. Also, additional experimental results have recently been published in Refs. 19 and 20.

II. Experimental Method

A. Test Facility

The NASA Ames 9x7 SWT is a closed circuit, continuous-flow, variable-density supersonic facility equipped with an asymmetric sliding-block nozzle that provides continuous Mach number adjustment from 1.54 to 2.56. Stagnation pressure can be varied from 634 to 4250 psf, with a maximum stagnation temperature of 600 °R. Over the operating envelope of the facility, the unit Reynolds number ranges from 0.9×10^6 to 5.8×10^6 per foot. Tunnel flow is produced using an 11-stage, axial-flow compressor powered by four variable-speed induction motors.[21] The nominal tunnel flow conditions utilized for this test are listed in Table 1.

Table 1. Nominal 9x7 SWT flow conditions

M_∞	Re_∞ (1/ft)	$T_{T\infty}$ (deg-R)	$P_{T\infty}$ (psf)	P_∞ (psf)	q_∞ (psf)
1.8	1.5E+06	550	800	140	317
2.4	1.5E+06	555	1060	74	295
2.4	1.0E+06	555	714	50	200

Grey fill = Overlap with LaRC test

The test section measures 9×7 feet in cross section and 18 feet in length with hatches in the ceiling and side of the tunnel for model access and installation. This large test section size allows for

higher thrust coefficients with reduced concern for tunnel blockage effects, which was a concern for the previous test.[11] A traversing horizontal strut spans the test section and contains the model support system with a knuckle-sleeve mechanism to position the test article at attitudes up to those circumscribed by a 15-degree half-angle cone. Bent adapters are available to alter the range of model angles. Typically, a model is pitched through angle of attack in the horizontal plane of the tunnel so that the traverse capability of the strut can be used to maintain the center of rotation near the tunnel centerline, as shown in the top view of Fig. 2. A 5-deg "dog-leg" adapter was utilized to acquire an alpha sweep of -10 to 20-deg. The 9x7 does not have a model roll mechanism, so the facility must be shut down to implement a manual model roll increment.

Two 28-inch-diameter windows in each sidewall at two different tunnel stations provide optical access for flow visualization techniques, as shown in the side view of Fig. 2. The forward window is at roughly tunnel station (TS) 130, while the rearward window is at TS 64. Each window is mounted offset in a 50-inch-diameter disk that can be manually rotated to vary the window position relative to the model and test section. These windows are used to acquire schlieren or shadowgraph data as the model traverses in the vertical plane during a β-sweep. With a center of rotation at the strut location (TS 0), the model can rotate quickly out of view of the 28-in diameter windows. For the present study, the model was installed within the rearward window, as shown in the side view of Fig. 2. The rearward location was used to shorten the model sting length and minimize the amount of vertical movement within the optical window.

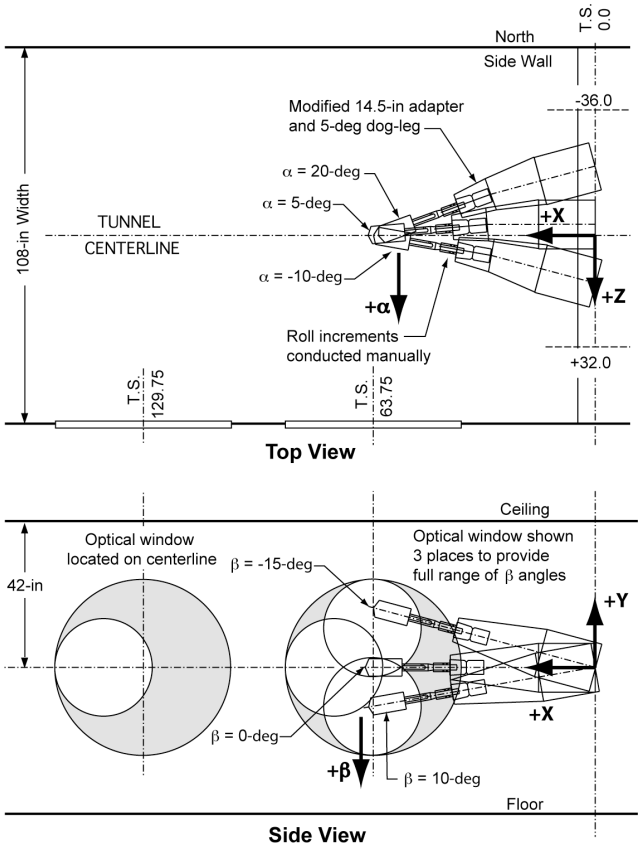

Figure 2 – Sketch showing model installed in the Ames 9x7 SWT

High-pressure air for jet simulations is supplied by dual, independently controlled auxiliary air systems at flow rates up to a total of 80 lb_m/sec at pressures up to 3000 psia. Air from one of these systems can be heated to temperatures up to 200 °F using a 1-MW heater. Flow rates are measured using sub-critical-flow venturi meters, while pressures and flow rates are regulated with a multi-poppet digital control valve (DCV).

B. Model

Reference 12 provides details of the model design, including a discussion of the internal flow and thermal analyses completed to insure that high quality data would be obtained. An oblique view of the final design in Fig. 3 shows a 5-in diameter SRP model comprised of a 70-deg sphere-cone forebody with locations for 4 nozzle or plug inserts followed by a cylindrical aftbody. The assembled model was designed with a partially hollow sting, as shown in cutaway sketch of Fig. 4, that feeds an internal plenum connected to each nozzle location via a four-fingered manifold. Note that the plenum is a constant diameter pipe with a 5-deg flare leading to the manifold. The predicted Mach number within the final plenum design is approximately 0.1 at worst-case conditions. The sting/plenum/manifold assembly provides the structural load path to hold the forebody with either

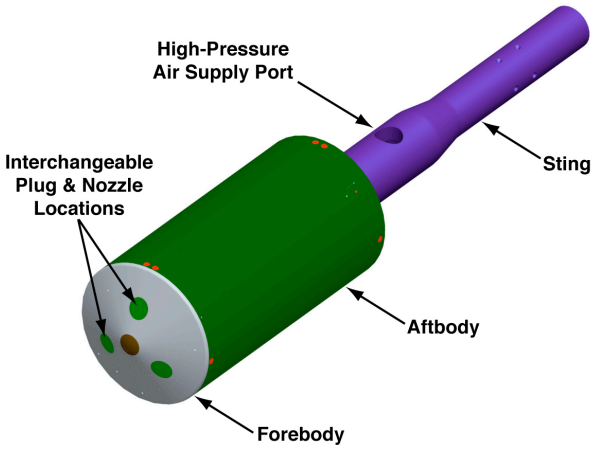

Figure 3 – Oblique view of UPWT SRP model assembly

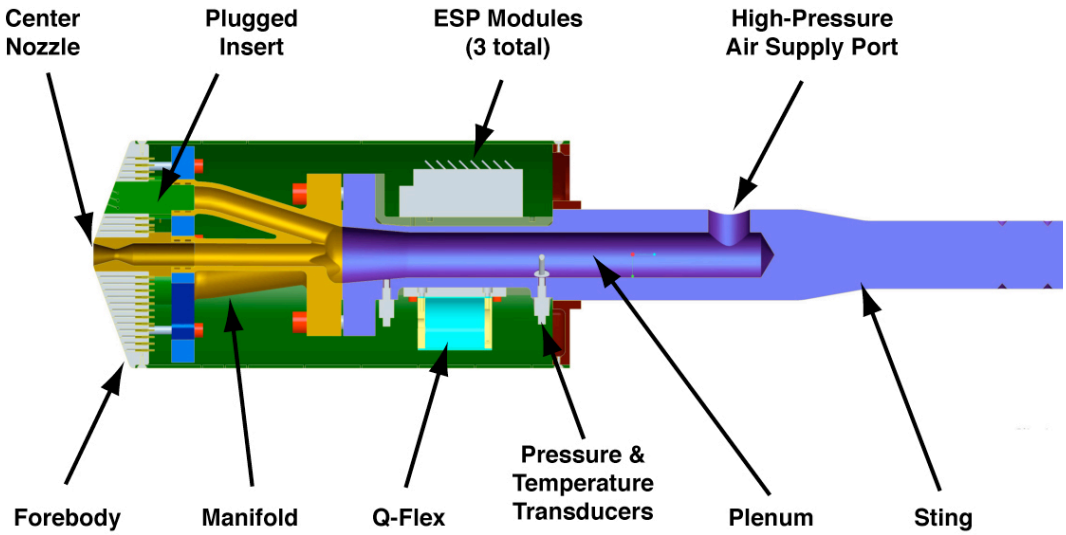

Figure 4 – Section view of the final design UPWT SRP model assembly

plugs or nozzles in place. The 9.55-in long aftbody, comprised of two thin-walled half cylinders attached as shown in Fig. 4, provides an enclosure to protect internal instrumentation and carries no load. Nozzle locations include one on model centerline and three on the forebody half-radius spaced 120° apart. The insert locations can host either 4:1 exit-to-throat area ratio conical nozzles or plugs that fit flush to the forebody, providing the baseline configuration. Configuration changes are accomplished by removing the un-instrumented side panel, then sliding the forebody forward (without disconnecting the ports) to replace the nozzle inserts.

C. Instrumentation

Experimental measurements were acquired at 167 surface pressure ports connected via 0.040-inch ID flexible urethane tubing to three 64-channel Pressure Systems Inc. (PSI) electronically scanned pressure (ESP) transducer modules located inside the model. The modules were rated for pressures from 0-15 ± 0.005 psid and used Digital Temperature Compensation (DTC) to correct each individual transducer for effects of thermal drift on the pressure measurements. The surface instrumentation layout is shown in Fig. 5. All three modules were teed to a fixed common reference pressure of 15 psia that was measured using a Paroscientific Model 1650 pressure transmitter (23 ± 0.002 psia). A PSI Model 8432 pressure calibration unit (PCU, 32.5 ± 0.003 psia) was used to provide a monitor pressure to four separate transducers on each ESP module to check for drift in the ESP pressure measurements.

Seven 0.0625-inch-diameter Kulite XCS-062-5A pressure transducers (0-5 ± 0.013 psia) with B-screens (to protect the sensing element) were mounted flush to the model forebody surface with adhesive potting material and

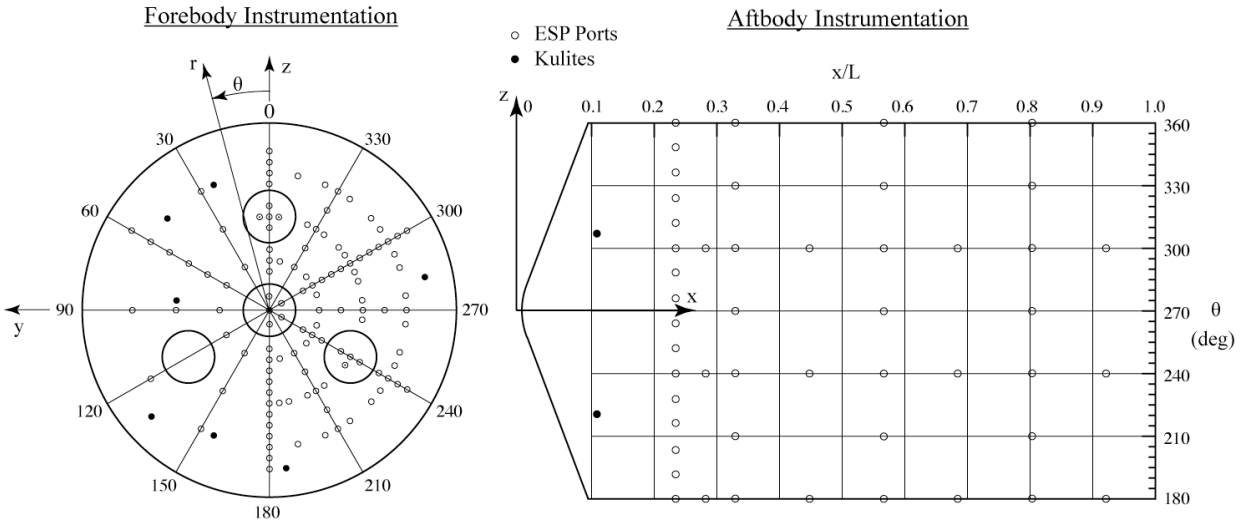

Figure 5 – Surface instrumentation layout and model coordinate system

used to measure fluctuating surface pressures. The locations of the Kulites are shown in Fig. 5 with filled circles. Two additional Kulite transducers were mounted in the model aft shell but were damaged during model assembly. Output signals from the Kulite gages were split to both standard and high-speed data acquisition systems to provide simultaneous time-averaged and unsteady pressure measurements.

Pressures were measured inside the model at different locations along the high-pressure airflow path using up to four Kulite XT-190-2000A pressure transducers (0-2000 ± 2 psia). Two transducers were located at different stations in the model plenum, with the gages mounted flush to the plenum inner surface. The remaining pressure transducers were connected to interior surface ports located 0.417 inches upstream of the nozzle inlets for the center nozzle and one of the half-radius nozzles. Figure 6 shows the center nozzle with pressure and temperature instrumentation. These transducers were active only when their respective nozzles were installed in the model.

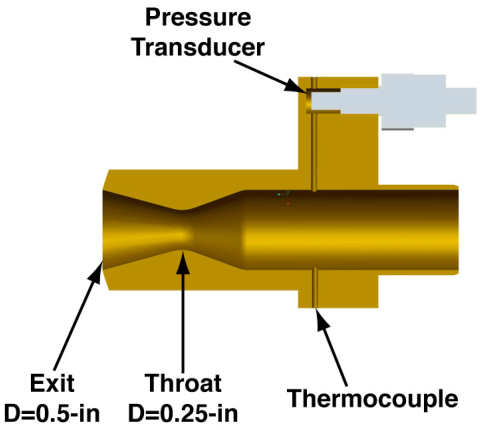

Figure 6 – Close up of the instrumented center nozzle

Plenum-flow temperatures were measured using a 0.236-in diameter Omega RTD-NPT-72-A platinum resistance temperature detector (RTD) probe (132-910 ± 1 R) located 0.5 inches into the high-pressure airflow (see Fig. 4). Additionally, each of the two instrumented nozzles contained a Type K thermocouple (132-2742 ± 4 R) mounted flush to the inside surface and opposite of the plenum pressure port.

A NASA Langley-built Q-Flex accelerometer was mounted inside the model and used to directly measure model pitch angle during the test. The device was calibrated in place as a function of pitch and roll angles using a multi-axis Angle Measurement System (AMS) installed on the model during setup. The resultant angular calibration accuracy was approximately ±0.01 degrees.

Eight Type K thermocouples (132-2742 ± 4 R) were installed to monitor the thermal environment inside the model during the test. A thermocouple was mounted underneath each ESP module and accelerometer, while the remaining four thermocouples were mounted inside the aft shell at approximately half the model length and every 90 degrees around its circumference.

A calibrated Flow Systems sub-critical venturi flow meter with 2.626-inch-diameter inlet and 1.970-inch-diameter throat was installed in the high-pressure air line and used to measure nozzle mass flow rate. The venturi inlet pressure was measured using a Paroscientific Model 1003KA pressure transducer (0-3000 ± 0.9 psia), while the inlet temperature was measured using a shielded Type 85 RTD probe with an accuracy of ±0.9 R. Pressure drop across the venturi throat was measured with a Rosemount Model 3051CD differential pressure transducer (0-26 ± 0.013 psid). Mass flow rate uncertainty is estimated to be approximately ±0.05 lbm/sec.

To capture flow field dynamics between bow and barrel shocks, a high-speed digital camera was utilized to record shadowgraph video. High quality images were acquired at 20,000 frames per second and then post processed into AVI movies.

D. Data Acquisition & Reduction

Model surface pressures measured with the ESP modules were acquired with the PSI 8400 System at a sampling rate of 10 Hz. The remaining data channels were also acquired at 10 Hz through the facility Standard Data System (SDS) and recorded at 16-bit analog-to-digital (A/D) conversion. Both systems used a sampling period of 2.5 seconds. Unsteady pressure data from the Kulite transducers were sampled at 40,000 Hz for a 2.525-second sampling period using the facility Dynamic Data System (DDS) synchronized to the SDS. These data were processed through a fixed analog filter to remove any frequency components beyond the range of the A/D converters, then digital filters to remove any frequency components above half the sampling rate before being digitized with a 24-bit A/D converter.

Raw voltages from the instrumentation were recorded and processed in real time (through respective calibration functions) into engineering unit values for real-time display, monitoring, and plotting. Facility flow conditions were calculated via standard gas dynamic equations using measured tunnel stagnation conditions and calibrated values of freestream Mach number. These flow conditions were then used to compute surface pressure coefficients, nozzle pressure ratios, nozzle exit-to-static pressure ratios, and nozzle thrust coefficients.

The measured plenum static pressures were corrected to total pressure values using total-to-static pressure ratios calculated from estimates of the plenum Mach number. These estimates were computed from a binomial approximation of the mass flow rate equation using the measured mass flow rates, plenum temperatures, and plenum cross section areas, and are valid for small Mach numbers. Model plenum and nozzle exit conditions were calculated using GASPROPS[22] to account for real-gas effects, the latter being based on plenum total conditions and nozzle area ratios. Real gas effects were estimated to be roughly 2% in C_T due to high pressure and low temperatures within the plenum. The thrust of each nozzle was computed from total measured mass flow rate and the ratio of individual nozzle throat area to total nozzle throat area.

Analysis of the DDS data was accomplished near real time during this test. Each DDS data file had 101,000 data points (40K samples per second for 2.525 seconds). A power spectral density (PSD) analysis was performed using the Welch method, which is a modified average of a periodogram. The data were broken into 10 blocks at 40,000 samples per block with 50% overlap. Each block was windowed using an amplitude-corrected Hanning window, which avoids leakage from non-periodic signals. This approach allowed for improved block averaging to reduce noise within the resulting analysis. The resulting frequency resolution using this approach is 1 Hz.

The model position was computed relative to the test section coordinate system for each set point based on axial and lateral model support system positions and pitch and yaw angles.

E. Run Matrix & Test Procedures

The run matrix is summarized in Table 2, in which the sequencing of parametric variation is listed in order from the most time consuming to implement to the least. The first step in the test was model assembly at the desired model roll angle and leak checking (the configuration of interest). Then, the tunnel was secured and the proper flow conditions established. If nozzles were installed, the next step was to set the desired thrust coefficient (by setting the desired plenum pressure and temperature). Then, the model was positioned at the proper location and orientation to begin the programmed angle of attack sweep. Once all desired locations were acquired, nozzle thrust was adjusted as appropriate for the next case in the run matrix. Finally, the tunnel flow conditions were adjusted as required. This sequence of events was repeated until all runs in the matrix were obtained, after which the tunnel was halted and opened to make the next model roll or configuration change. Pressure module calibrations were conducted after every configuration change, and as needed to check and/or adjust for temperature drift of the module.

Table 2. Sequence of parametric variation for UPWT SRP test

Step	Parameter of Interest	Typical Settings
1	Set Model Configuration and Roll Increment	Baseline, Center, Tri, Quad Roll = 0 & 180, 30 & 210*
2	Set Tunnel Flow Conditions	M=1.8/Re=1.5, M=2.4/Re=1, M=2.4/Re=1.5
3	Set Nozzle Thrust	C_T = 0, 2, 4, 6, 8, 10
4	Set Model Position	Z=0, ±12, ±24
5	Conduct Alpha Sweep in the horizontal plane	α = 0, ±4, ±8, 12, 16, 20
6	Conduct Beta Sweep in the vertical plane for schlieren	β = 0, 4, 8, 12

* limited cases

The model allows for four basic configurations, as listed in Table 2: (1) baseline, with all four nozzle inserts plugged; (2) center nozzle, with the three peripheral locations plugged; (3) tri-nozzle, with only the center plugged; and (4) quad-nozzle, with no plugs. During pre-test planning, the first three configurations were deemed a high priority for this test entry, while the quad configuration was considered a lower priority. In the end, all four configurations were tested.

To minimize the number of tunnel conditions while maximizing thrust coefficient, only the lowest attainable Reynolds number was considered for the full range of Mach numbers. Thus, freestream unit Reynolds number was 1.5×10^6/ft for a majority of the test. However, a lower Re_∞ of 1.0×10^6/ft was also acquired at Mach 2.4 to provide overlap with the previous test entry at NASA Langley. The Mach number sweep was considered a high priority for this test entry, providing both overlap and an extension of the database at supersonic conditions.

When nozzles were installed, the plenum pressure was controlled and adjusted via the DCV, with fixed temperatures near 135-degF, to provide the desired thrust coefficients listed in Table 2. This temperature was more than 40-degF above the liquefaction limit for flow within the nozzles. Considering the intent of this study, a full range of thrust coefficients was considered a high priority. The larger test section size enabled a wider range of thrust coefficients (up to 10), with the exception of the center nozzle case which was restricted to C_T of 4 and below due to pressure limits. For the center nozzle, C_T of 2, 3, and 4 were acquired.

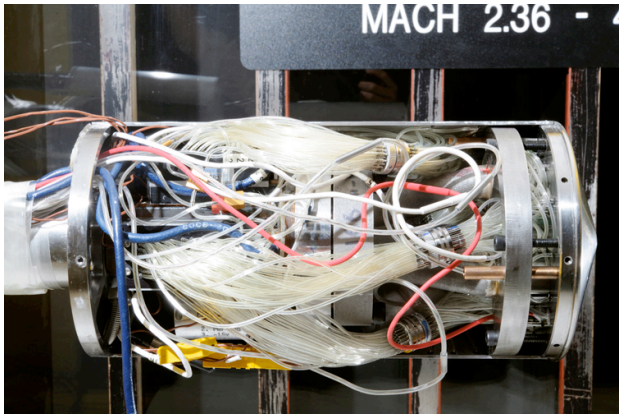

Figure 7 – Internal pressure lines and instrumentation wiring

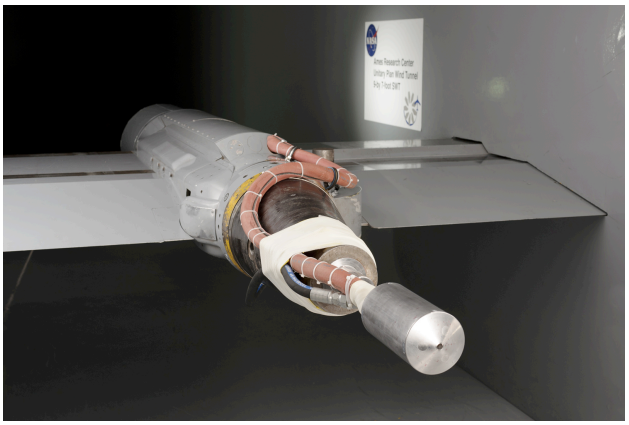

Figure 8 – Model installed in the Ames 9x7-Foot SWT

The largest allowable range of lateral (Z) model translations was considered important for uncertainty estimation, especially for the baseline configuration, by providing repeatability data from different locations within the tunnel. Notional model translation locations are listed in Table 2. The 9x7 traversing-strut does not provide the capability to travel in the longitudinal (X) or vertical (Y) directions.

Due to the lack of a model roll mechanism with the standard tunnel hardware, the number of model roll cases was reduced to angles of 0 and 180-deg, although a few runs were acquired of the tri and quad-nozzle configurations at 30 and 210-deg. These off nominal cases were conducted for the multi-nozzle, or non-axisymmetric, cases primarily for flow visualization to allow comparison against the previous[11] data set.

For the α-sweep, the tunnel angle-of-attack mechanism was programmed to pause at 0, ±4, ±8, 12, 16, and 20-deg. The typical sweep sequence included nine pause points, starting at -8-deg and proceeding to 20-deg, followed by 0-deg repeat. For flow visualization runs, the vertical plane was used to acquire β-sweeps from 0 to 12 deg in 4-deg increments, as noted as the last step in Table 2.

Figure 7 provides a photo of the internal volume of the model (with one half of the afbody removed) showing the manifold, pressure tubing, and thermocouple wires. Figure 8 provides an installation photo of the center-nozzle configuration, which shows the tunnel hardware, high-pressure-air line, and instrumentation wiring bundles. Note that all connections to the model required extra slack to allow a full range of motion without binding. Before installation into the tunnel, a pressure qualification test of the model was performed to 3750 psia, which allowed for safe operating pressures up to 2500 psia. The tunnel, however, had relief valves for their high-pressure system set to 2350 psia.

Discussion of Results

The test began in the Ames 9x7 SWT on August 8th, 2011 and lasted roughly two weeks. Over 300 runs were acquired during the test and most primary test objectives were accomplished; exceptions will be discussed in the following sections. A comparison of sample results at the beginning of the test led to the decision to use the shadowgraph technique, instead of schlieren (which was used at LaRC), for flow visualization. Shadowgraph provided clearer images of the nozzle flow, while schlieren proved too sensitive to Mach lines from the tunnel wall. The results contained herein represent a quick look at trends and observations gleaned from the shadowgraph and pressure results, highlighting some key observations that are unique to this dataset.

All four configurations were tested: 1) baseline, with no nozzles, 2) center nozzle, with the peripheral nozzles blocked, 3) tri-nozzle, with only the center blocked, and 4) quad-nozzle, with none blocked. The baseline configuration data was mainly acquired to allow quantification of various sources of experimental uncertainty, which will be discussed in a separate paper, with the exception of the flow calibration effort in the next section. Results from the other three configurations will be discussed subsequently.

F. Flow Calibrations

Similar to the earlier LaRC test, tunnel flow quality and optical access were important considerations discussed during pre-test planning meetings. The decision was made to locate the model within the rearward optical window to maximize the range of angles of attack for viewing the interaction dynamics with a high-speed camera. This location was significantly downstream of standard model positions, and as it turned out, not a location that had been previously calibrated. The assumption was that the relatively linear behavior of the calibration data with model

position could be extrapolated to this new downstream location. This assumption turned out to be erroneous. When the initial baseline data became available, comparisons against the previous LaRC results (at the overlap condition of Mach 2.4 and Re_∞=1.0x10^6/ft) and pre-test computations revealed an offset that suggested a flow calibration issue. Figure 9 provides an example of the initial steady surface pressure coefficient measurements on the baseline (no nozzle) configuration at Mach 2.4 and Re_∞=1.0x10^6/ft, revealing the Ames data to be significantly higher than the LaRC data and post-test computations. Note that this initial stagnation point value is slightly over 2% higher than the maximum stagnation point pressure coefficient as calculated from Newtonian theory.

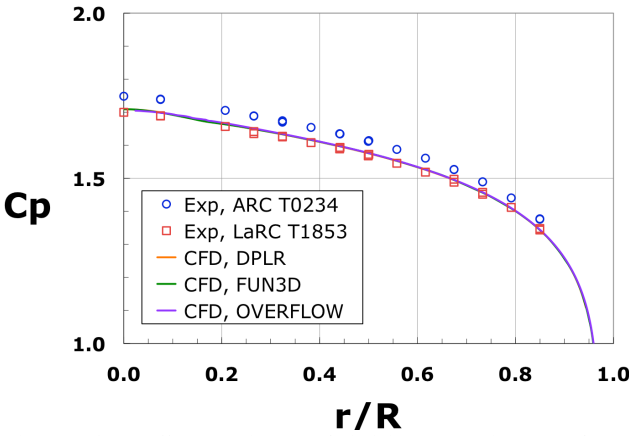

Figure 9 – Comparison of initial baseline surface pressure data against computations and previous data for M_∞=2.4, Re_∞=1.0x10^6/ft, and α=0-deg

As a result of these initial comparisons, a request was made to verify the tunnel calibrations for the model station that was used for this study. A post-test survey was conducted of the Mach number using a single Pitot tube located and traversed along the horizontal centerline, as shown in Fig. 10, for the range of present test conditions. An example of the resulting survey conducted for the

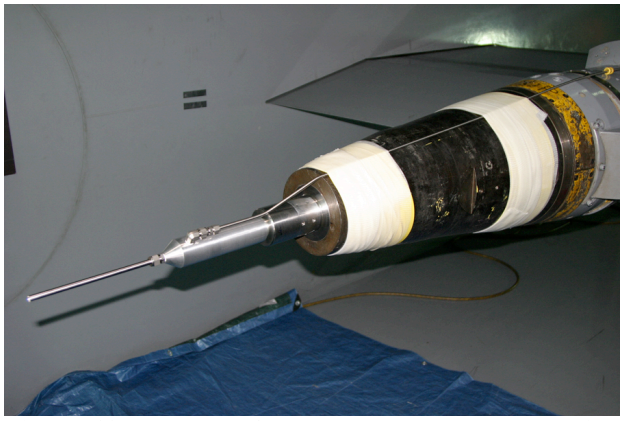

Figure 10 – Photo of the Mach probe used during post-test calibrations

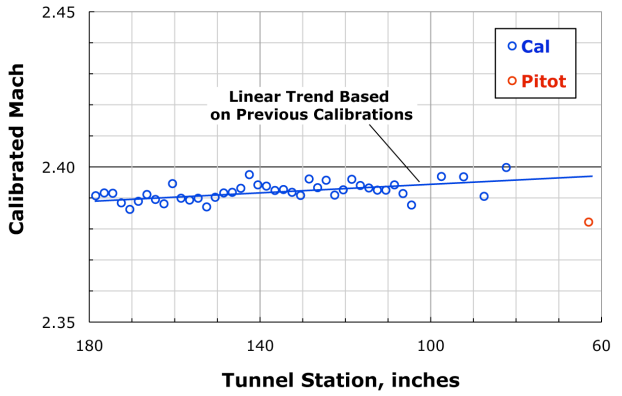

Figure 11 – Tunnel centerline calibration results at M_∞=2.4 and Re_∞=1.0x10^6/ft

range of previous calibrated locations against the new data point is shown for the horizontal centerline in Fig. 11 for Mach 2.4 and Re_∞=1.0x10^6/ft, indicating that indeed the resulting Mach number at model station 63 is lower than a linear extrapolation of the older data. The red data point in this plot is the new calibration result, as compared against the older Mach calibrations at the forward stations in blue.

Figure 12 provides the same data shown earlier, but now re-plotted using the new TS 63 tunnel flow calibration. As can be seen, the new calibration brings the Ames baseline data into better agreement with computations and the Langley data, especially at the stagnation point. The plotted symbol sizes provide a rough estimate of the experimental uncertainty determined from an analysis of the Langley data.[19] The divergence towards the shoulder region could be due to a difference in flow angularity between the two tunnels. All data presented herein have been reduced using the new TS 63 calibration data. An uncertainty assessment, similar to the one provided in Ref. 19, is presently on going and will be contained in a separate report.

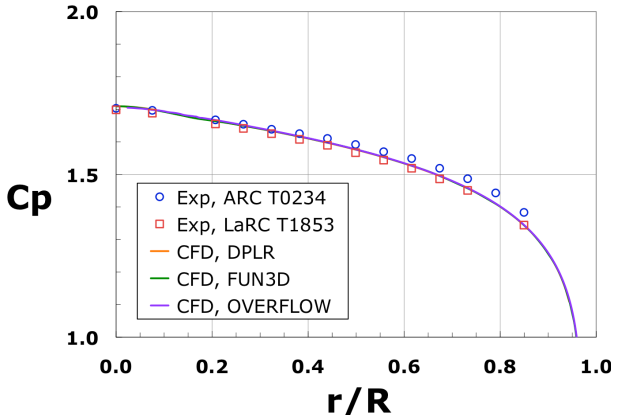

Figure 12 – Comparison of re-computed baseline pressure data against computations and previous data for M_∞=2.4, Re_∞=1.0x10^6/ft, and α=0-deg

G. Center Nozzle

The center nozzle represents the simplest SRP configuration from a computational perspective,[13] and an important segment of this experiment. Thus, all primary center-nozzle objectives were completed during the test. The thrust range was limited for the center nozzle, due to the pressure limit of 2350 psi, with C_T's of 0, 2, 3, and 4 acquired. The model was rolled to both the 0 and 180-deg positions.

Figure 13 provides shadowgraph results for a sweep of angles of attack obtained for the center nozzle at Mach 2.4 with a C_T of 4. These images are a result of processing to provide an average of the sequence of all frames taken during each test point. Image averaging in this manner filters out most flow field fluctuations such that any features left behind can be assumed to be steady, or quasi steady, in time. The level of steadiness is reflected by the sharpness of the features in these images: quasi-steady or periodic appear only slightly blurry, while chaotic features completely disappear. In Fig. 13, the barrel and bow shocks can be seen, for the most part, to be very steady for this center nozzle case. The most obvious location for unsteadiness, as determined by the lack of definition in these averaged images, is restricted to the triple point region, especially for the higher angle of attack cases. The observation of local unsteadiness at the triple point for the center nozzle is consistent with the results previously published[11] from the LaRC test.

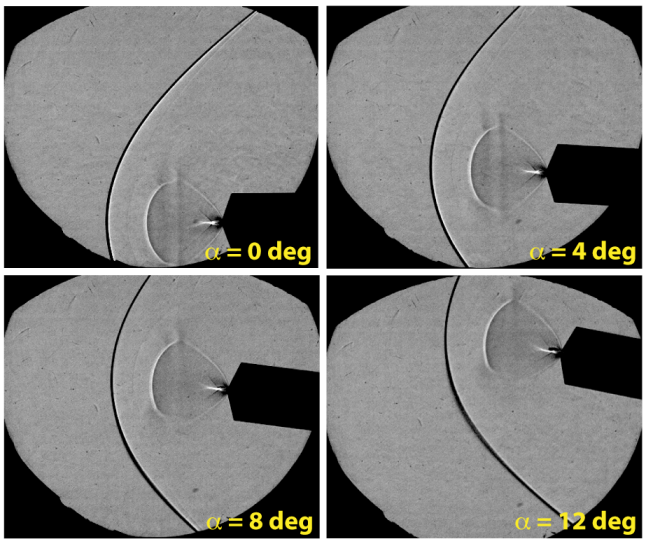

Figure 13. Effect of angle of attack showing steady features for the center nozzle at M_∞=2.4, Re_∞=1.5x10^6/ft, and C_T=4

To further explore the dynamics of the interactions formed by a single barrel shock responding to the freestream, Fig. 14 provides a time-step sequence for a typical triple-point periodic cycle for both the α = 0 and 12 deg cases at Mach 2.4 and C_T of 4. Figure 14a presents, for α = 0 deg, an example of a smaller "wave-like" triple point oscillation[17] and the complete cycle appears to repeat every 0.8 ms (roughly). Although the lower portion is partially obscured by the window frame, it does appear that the wave formation and roll over occurs symmetrically along the periphery of the annular triple-point. This wave-like structure has previously been described as ring-vortex shedding based on in-depth review of the dynamics observed in the computational solutions.[13] Vortex shedding on a cycle of one every 0.8ms corresponds to a frequency of 1.25kHz. The dynamic data analysis identified a small peak on all forebody sensors at 1.3kHz for this case. When the model is pitched up to α = 12 deg,

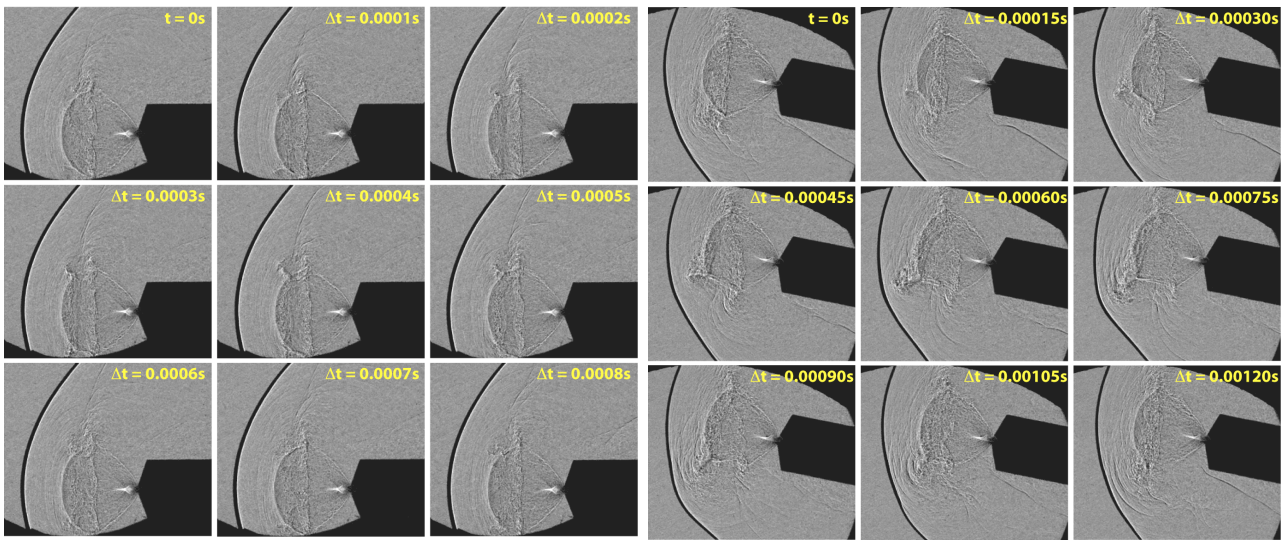

a) α = 0 deg **b) α = 12 deg**

Figure 14. Periodic behavior for two angles of attack for the center nozzle at M_∞=2.4, Re_∞=1.5x10^6/ft, and C_T=4

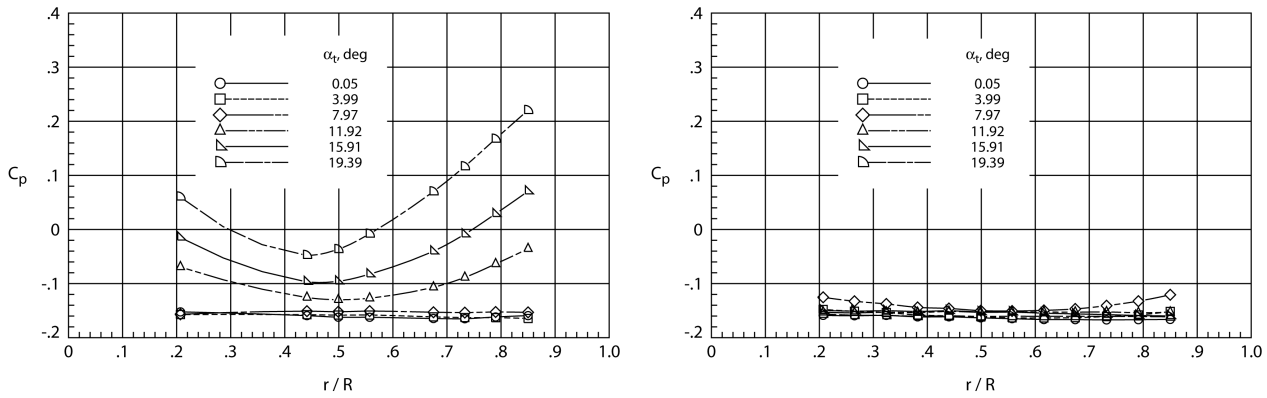

a) Windward ray **b) Leeward ray**

Figure 15. Effect of angle-of-attack on center nozzle forebody pressures at M_∞=2.4, Re_∞=1.5x10^6/ft, and C_T=4

Fig. 14b, the periodic behavior appears to centralize around the windward triple point region and the cycle lengthens to roughly 1.2 ms. Vortex shedding on a cycle of one every 1.2ms corresponds to a frequency of 0.83kHz. The dynamic data analysis identified a frequency of 0.88kHz for this case. The observation of a longer periodic cycle with increasing angle of attack is consistent with trends provided in Ref. 17, whereby the calculated frequency of oscillations in the force coefficients (see Fig. 10 of Ref. 17) were found to decrease with increasing α. The decreased frequency corresponds to an increase in the size of the wave crest, to the point of actually affecting the bow shock slightly (note the bulge in Fig. 14b, Δt of 0.6ms and beyond). The periodic bulging of the bow shock does result in a slight blurring (or thickening) of the bow shock shown in the lower right averaged image of Fig. 13. Looking at all angles of attack, the dynamic data reveals a nearly linear trend of a decreasing shedding frequency with increasing α for this center nozzle case.

Sample forebody pressure data corresponding to the full angle of attack range (in the horizontal plane) of the center nozzle configuration at Mach 2.4, Re_∞=1.5x10^6/ft, and C_T=4 is provided in Fig. 15. The windward ray is provided in Fig. 15a, showing that even for this moderate thrust level (C_T=4), the forebody is highly separated up to an angle of attack of 8-deg. As the angle of attack increases further, pressure levels on the shoulder and near the jet exit systematically elevate above the separated level. Figure 14b provides evidence of a compression shock emanating from the windward shoulder region for the α = 12 deg case. The leeward ray, on the other hand, remains separated for entire range of angles of attack, as shown in Fig. 15b.

H. Tri Nozzle

The tri-nozzle was the prime multi-nozzle configuration, thus most objectives were completed during the test. The only exception being the ϕ = 0-deg cases, which were substituted with ϕ = 30 and 210-deg cases for better

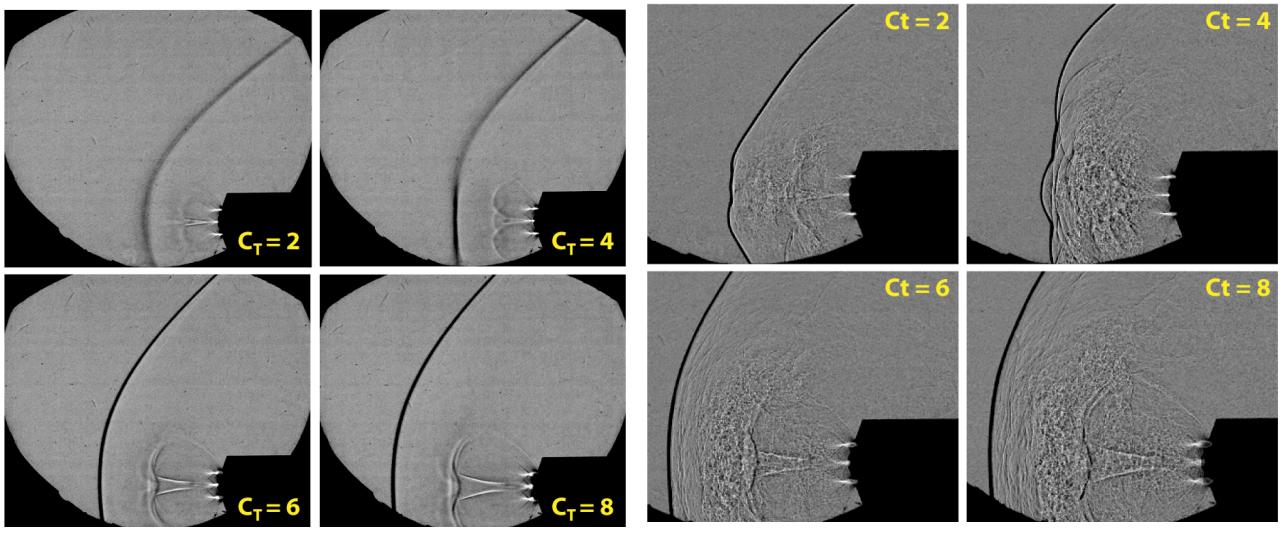

a) Averaged images. **b) Instantaneous and zoomed-in images.**

Figure 16. Effect of thrust coefficient for the tri nozzle at M_∞=2.4, Re_∞=1.5x10^6/ft, ϕ=180-deg, and α=0-deg

comparison to the LaRC data (discussed earlier). Data were acquired for all test conditions, angles of attack, and thrust coefficients (up to 10).

Figure 16 provides shadowgraphs, both averaged and instantaneous images obtained from the video, for a series of thrust coefficients obtained for the tri nozzle configuration at Mach 2.4 with α = 0 deg. From the average images in Fig. 16a, one can note that at lower thrust, the bow and barrel shocks are slightly blurry, indicating some unsteadiness. The blurred bow shocks in the average images of Fig. 16a correspond to the irregular shaped bow shocks of the instantaneous images of Fig. 16b. But as thrust is increased, the shocks become sharper in the average images, thus an indication of steadier behavior. Also from both sets of images, one can observe that the formation of an organized central feature within the region between the three barrel-shocks at C_T of 6 and above leads to a further thrusting out of the bow shock and steadier behavior. This feature (resembling a sideways "V" with an inverted sombrero on the end) is believed to be, based on an examination of the computational results for a similar case presented in Ref. 17, the internal plume boundary of the two side-by-side barrel shocks. At the higher thrust levels, the internal plume boundary appears to develop a thick shear layer that feeds the internal turbulence seen to spill out in front of the Mack disk region in Fig. 16b. This observation of increased steadiness as thrust increases is counter to what was published for the Langley results with the tri-nozzle configuration. In the earlier study, thrust coefficients were limited to below 5 due to wall interference concerns, which is approximately the point at which the flow structures tend to become steady with the Ames data. Even at the highest thrust coefficient (C_T = 10), shown in Fig 17, the flow structures remain steady even over the observable angle of attack range. The conclusion from the previous paper of flow unsteadiness at higher thrust seemed counter intuitive and has now

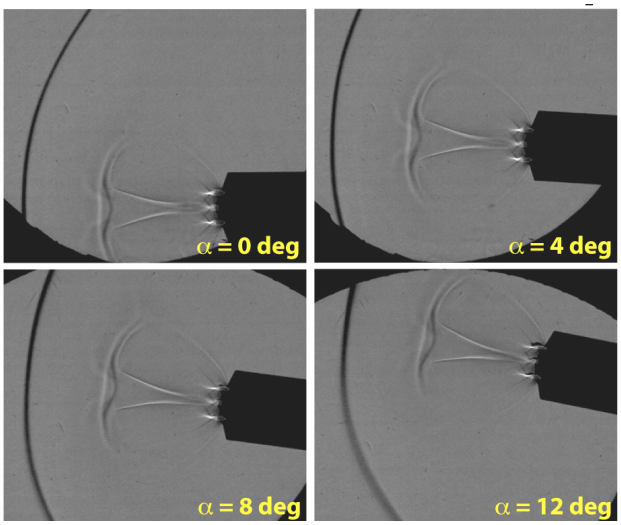

Figure 17. Effect of angle of attack for the tri nozzle at M_∞=2.4, Re_∞=1.5x10^6/ft, ϕ=180-deg, and C_T=10

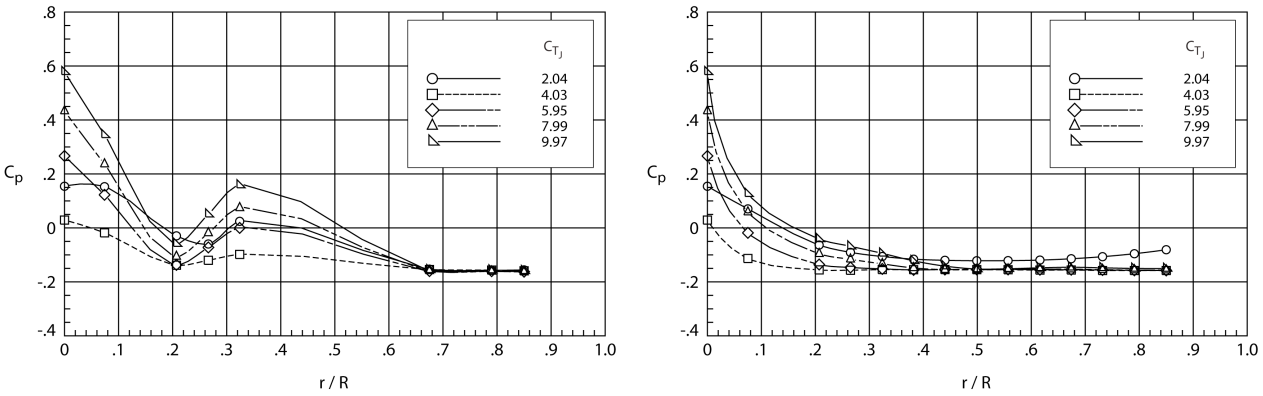

a) θ=0-deg ray **b) θ=180-deg ray**

Figure 18. Effect of thrust on tri nozzle forebody pressures at M_∞=2.4, Re_∞=1.5x10^6/ft, and α = 0 deg

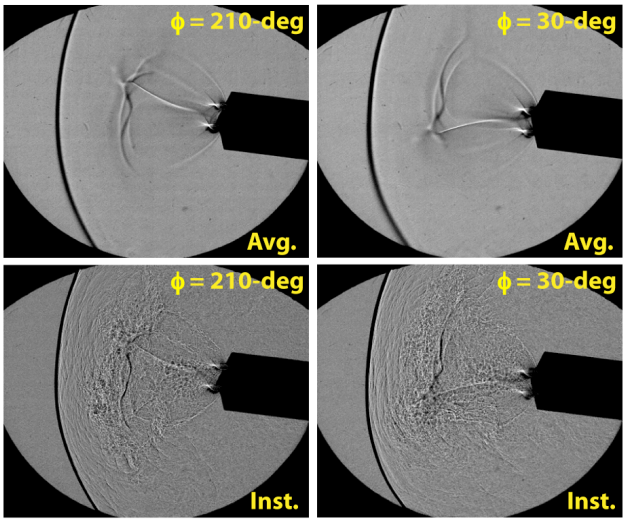

Figure 19. Effect of model roll for the tri nozzle at M_∞=2.4, Re_∞=1.5x10^6/ft, α = 8-deg, and C_T=10

been shown to be an incomplete observation for the tri-nozzle configuration.

The pressure coefficient data, for 2 representative forebody rays, corresponding to the range of thrust coefficient cases presented in Figs 16 and 17 for M_∞=2.4, Re_∞=1.5x10^6/ft, ϕ=180-deg, and α=0-deg are provided in Fig. 18. The forebody is highly separated for the range of thrust cases shown, but the pressure does increase in the stagnation region between the nozzles and on the inside edge of the nozzle as the thrust level increases.

The average images in Fig. 17 suggest that the flow field remains steady up to the highest thrust tested for the observable range of angles of attack. Since the roll axis during the Ames test was rotated 90-deg in relation to the optical view angle (0 roll was set for positive angle of attack in the horizontal plane, not the vertical plane that was used for the shadowgraph), the standard view (ϕ = 0 or 180 deg) provided for three distinct barrel shocks in the images. For this reason, a late request was made for additional roll angles, to allow for direct comparison against the LaRC data. Figure 19 compares these two roll angles for the tri nozzle at Mach 2.4, α = 8 deg and C_T = 10. A model roll of 30-deg provides for a single nozzle on the windward side (lower half) of the model. With this orientation, the lower barrel shock loses definition in the averaged image, an indication of unsteadiness. The corresponding instantaneous image reveals a lower barrel shock with an ambiguous, or ill-defined, triple point, perhaps one in the middle of a large-scale oscillation. A model roll of 210-deg provides for two nozzles on the windward side. This orientation provides a more distinct barrel shock in the averaged image, suggesting steadier behavior. The corresponding instantaneous image reveals a fuller windward barrel shock, but does suggest a small oscillation at the triple point. In either case, while the windward triple point regions does appear to be a source of unsteadiness for both orientations, the bow shock structure does not seem to be adversely affected. From the dynamic data analysis of the cases shown in Figs. 17 and 19, no clear trend was observed in reference to model roll. There was a repeatable trend with angle of attack, with peak frequencies around 0.6kHz for all sensors at α = 0-deg that slowly decreased to around 0.4kHz for most windward sensors at α = 12-deg. Unfortunately, the high angle of attack mode-switching behavior due to model roll (as reported in Ref. 11 for the quad nozzle case) could not be investigated during the Ames test due to the optical viewing restriction of α = 0 to 12-deg.

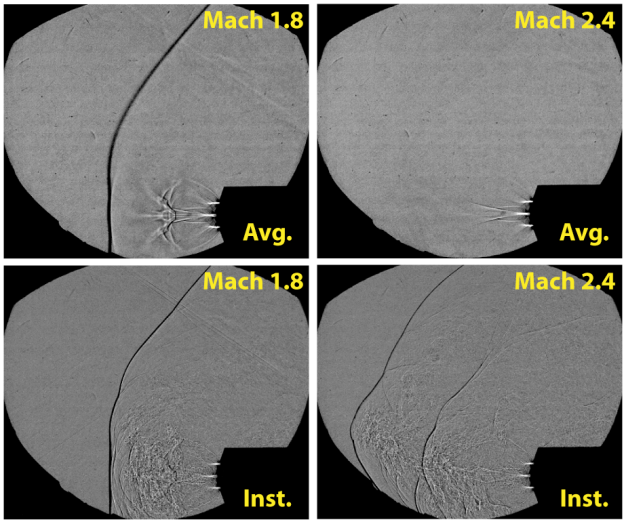

Figure 20. Effect of Mach number for quad nozzle at α = 0 deg, Re_∞=1.5x10^6/ft, ϕ = 0 deg, and C_T=4

I. Quad Nozzle

The quad nozzle was the lowest priority configuration, so not all objectives could be accomplished during the test. Data were acquired for all test conditions, angles of attack, and thrust coefficients (up to 10), but only for ϕ = 0-deg. The planned ϕ = 180-deg cases were dropped for lack of time during the 2 week entry, and there was no attempt to look at the off nominal roll cases.

The quad nozzle results from the Ames entry also led to different conclusions than previously published. Figure 20 provides an example, showing both the averaged and an instantaneous image for the quad nozzle for a C_T of 4 and α = 0 deg for Mach numbers of 1.8 and 2.4. At the lower Mach number, the bow and barrel shocks are fairly steady and reveal an unusual feature just upstream of the multiple Mach termination disks. This unusual feature, best described as a tripod with legs pointing towards the bow shock, was seen previously during the LaRC test and appears to be the result of additional shock

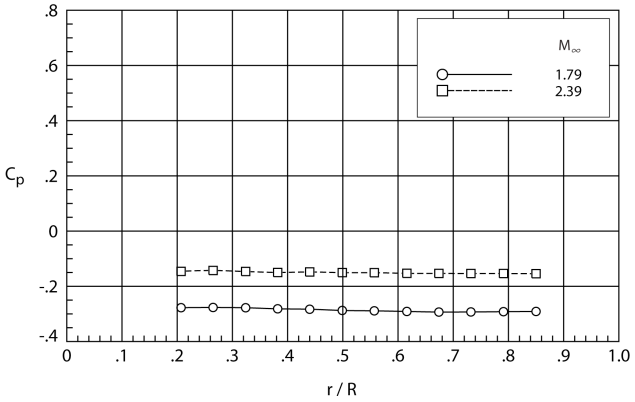

Figure 21. Effect of Mach number on quad-nozzle forebody pressures at α = 0 deg, Re_∞=1.5x10^6/ft, ϕ = 0 deg, and C_T=4

processing due to the addition of the central barrel shock. The feature is more difficult to see in the instantaneous image due to localized turbulence just in front of the barrel shocks. As Mach is increased to 2.4, this additional feature, along with the bow and most of the barrel shock disappear in the averaged image, an indication that the flow has become highly unsteady. The instantaneous image reveals the flow to be highly chaotic for the Mach 2.4 case. Figure 21 provides the corresponding pressure data on the θ=180-deg ray (between the nozzles) and reveals the forebody to be highly separated for both cases. Both Mach numbers exhibit the chaotic bow shock behavior at the higher thrust coefficients, although for the lower thrust, the flow reverts back to quasi–steady behavior as the angle of attack increases. The trend of large scale flow unsteadiness at higher thrusts was not seen at Langley due to the thrust coefficient cases being limited to values no higher than 3 due to time constraints. Thus the quad-nozzle configuration has now been shown to only provide steady or quasi-steady behavior at the lower thrust coefficients.

Summary

Supersonic retropropulsion is a potentially enabling technology for future heavy payloads to Mars and has been the focus of the Entry, Descent, and Landing community for the past few years. The present paper provides an initial review of the results obtained during the second of two planned entries into NASA supersonic facilities to acquire code validation quality data. This second test, into the ARC 9x7-Foot Supersonic Wind Tunnel, was conducted at Mach 1.8 and 2.4, the higher Mach providing overlap with the previous test conducted in the LaRC Unitary Plan Wind Tunnel. The model consisted of a 5-in diameter 70-deg sphere-cone forebody followed by a roughly 10-in long cylindrical aftbody. The forebody was designed to allow placement of up to four 4:1 area ratio conical nozzles connected up to the facility high-pressure air handling system. Instrumentation included surface pressures, both steady and high-speed, and flow visualization, in the form of high-speed shadowgraph to visualize the bow and nozzle shock interaction dynamics.

This test entry provided both overlap data with the previous test as well as an extension of the code validation data set to lower Mach numbers and higher thrust coefficients. Once the tunnel flow conditions were recalibrated for the model station used for the present study, the overlap data was shown to be in excellent agreement with the previous data and computations. The supplemental data proved to be very valuable as it was shown that previous conclusions from the multi nozzle cases were premature. In particular, the higher thrust conditions ($C_T > 5$) with the tri-nozzle were found to be quite stable even at moderate angles of attack, contradicting the observations reached at the conclusion of the limited Langley entry. Additionally, for the quad nozzle, it was shown that for thrust levels higher than achieved previously provided highly chaotic bow and barrel shock interactions.

In terms of general SRP conclusions inferred from this test campaign, a single central nozzle provides, for the same thrust, a bigger and more stable jet plume than the multi nozzle configurations tested, and the bow shock is pushed further away from body and also is more stable. If angle of attack is desired or required, the central nozzle also provides an advantage in that it allows for a wider range of α with acceptable steady behavior (only minor triple point oscillations that do not adversely affect the bow shock), although the multi jet configurations could be used to get a very stable flow field at extreme angles of attack (α of 16 or 20 deg). For multi-nozzle configurations, the present data set may not represent the optimum configuration in terms of number and placement of the nozzles. Further studies of multiple jet configurations are recommended.

Acknowledgments

The authors would like to acknowledge the support of NASA's Exploration Technology Development and Demonstration (ETDD) Program and Fundamental Aeronautics Program (FAP). The work documented herein was performed jointly by both ETDD's Entry, Descent, and Landing (EDL) Technology Development Project and FAP's Hypersonics Project, both managed at NASA-Langley Research Center. Furthermore, the following individuals were instrumental to this experimental effort: Joe Giuliana, Paul Tucker, Kerry Trumble, Artem Dyakonov, Josh Codoni, Chris Cordell, Guy Schauerhamer, Ashley Korzun, Jennifer Everett, Max Amaya, Tom Bridge, James Brown, Bill Browning, Jay Carolino, Maureen Delgado, Joel Hoffman, John Holmberg, Rudy Jaklitsch, Matt Krakenburg, David Lam, Pam Pfohl, Scott Richey, Tom Romer, Nestor Rostran, Art Silva, Robin Townsend, Dale Tuttle, Jonathan VanHorn, Bill VanZuylen, and Tom Volden.

References

[1] Braun, R. D., and Manning, R. M., "Mars Exploration Entry, Descent, and Landing Challenges," *Journal of Spacecraft and Rockets*, Vol. 44, No. 2, 2007, pp. 310–323.

[2] Steinfeldt, B. A., Theisinger, J. E., Korzun, A. M., Clark, I. G., Grant, M. J., and Braun, R. D., "High Mass Mars Entry, Descent, and Landing Architecture Assessment," AIAA Paper 2009-6684, Sept. 2009.

[3] Zang, T. A., and Munk, M. M., et al., "Entry, Descent and Landing Systems Analysis Study: Phase 1 Report," NASA TM 2010-216720, July 2010.

[4] Edquist, K. T., Dyakonov, A. A., Korzun, A. M., Shidner, J. D., Studak, J. W., Tigges, M. A., Kipp, D. M., Prakash, R., Trumble, K. A., Dupzyk, I. C., "Development of Supersonic Retro-Propulsion for Future Mars Entry, Descent, and Landing Systems," AIAA Paper 2010-5046, June 2010.

[5] Korzun, A. M., and Braun, R. D., "Performance Characterization of Supersonic Retropropulsion for High-Mass Mars Entry Systems," *Journal of Spacecraft and Rockets*, Vol. 47, No. 5, pp. 836-848, 2010.

[6] Korzun, A. M., Braun, R. D., and Cruz, J. R., "Survey of Supersonic Retropropulsion Technology for Mars Entry, Descent, and Landing," *Journal of Spacecraft and Rockets*, Vol. 46, No. 5, 2009, pp. 929–937.

[7] Korzun, A., "Aerodynamic and Performance Characterization of Supersonic Retropropulsion for Application to Planetary Entry and Descent," Ph. D. Dissertation, Department of Aerospace Engineering, Georgia Institute of Technology, Atlanta, GA, 2012.

[8] Jarvinen, P. O., and Adams, R. H., "The Aerodynamic Characteristics of Large Angled Cones with Retrorockets," NASA CR NAS 7-576, Feb. 1970.

[9] Trumble, K. A., Schauerhamer, D. G., Kleb, W. L., Carlson, J-R., Buning, P. G., Edquist, K. T., and Barnhardt, M. D., "An Initial Assessment of Navier-Stokes Codes Applied to Supersonic Retro-Propulsion," AIAA Paper 2010-5047, June 2010.

[10] Aeschliman, D. P. and Oberkampf, W. L., "Experimental Methodology for Computational Fluid Dynamics Code Validation," AIAA Journal, Vol. 36, No. 5, May 1988, pp. 733-741.

[11] Berry, S.A., Rhode, M.N., Edquist, K. T., and Player, C. J., "Supersonic Retropropulsion Experimental Results from the NASA Langley Unitary Plan Wind Tunnel," AIAA Paper 2011-3489, June 2011.

[12] Berry, S.A., Laws, C.T., Kleb, W.L., Rhode, M.N., Spells, C., Mccrea, A.C., Trumble, K.A., Schauerhamer, D.G., Oberkampf, W.L., "Supersonic Retro-Propulsion Experimental Design for Computational Fluid Dynamics Model Validation," IEEE Aerospace Conference Paper No.1499, March 2011.

[13] Trumble, K., Schauerhamer, D.G., Kleb, W., Carlson, J-R, Edquist, K., "Analysis of Navier-Stokes Codes Applied to Supersonic Retro-Propulsion Wind Tunnel Test," IEEE, paper #1471, March 2011.

[14] Kleb, W. L., Carlson, JR., Buning, P. G., Berry, S. A., Rhode, M. N., Edquist, K. T., Schauerhamer, D. G., Trumble, K. A., Sozer, E., "Toward Supersonic Retropropulsion CFD Validation," AIAA Paper 2011-3490, June 2011.

[15] Korzun, A. M., Clark, I. G., and Braun, R. D., "Application of a Reynolds-Averaged Navier-Stokes Approach to Supersonic Retropropulsion Flowfields," AIAA Paper 2011-3193, June 2011.

[16] Bakhtian, N. M., and Aftosmis, M. J., "Analysis of Inviscid Simulations for the Study of Supersonic Retropropulsion," AIAA Paper 2011-3194, June 2011.

[17] Schauerhamer, D.G., Trumble, K.A., Kleb, W., Carlson, J.R., and Edquist, K.T., "Continuing Validation of Computational Fluid Dynamics for Supersonic Retropropulsion," AIAA Paper 2012-0864, Jan. 2012.

[18] Trumble, K., Schauerhamer, D.G., Kleb, W., Carlson, J-R, Edquist, K., "Computational Fluid Dynamics Validation and Post-test Analysis of Supersonic Retropropulsion in the Ames 9x7 Unitary Tunnel," to be published at the 42nd AIAA Fluid Dynamics Conference, New Orleans, LA, June 2012 (pending publication).

[19] Rhode, M.N. and Oberkampf, W.L., "Estimation of Uncertainty for a Supersonic Retro-Propulsion Model Validation Experiment in a Wind Tunnel", to be published at the 42nd AIAA Fluid Dynamics Conference, New Orleans, LA, June 2012 (pending publication).

[20] Codoni, J.R. and Berry, S.A., "Analysis of High Frequency Data from Supersonic Retropropulsion Experiments in the NASA Langley Unitary Plan Wind Tunnel," to be published at the 42nd AIAA Fluid Dynamics Conference, New Orleans, LA, June 2012 (pending publication).

[21] "Test Planning Guide for High Speed Wind Tunnels, Rev 5," http://www.windtunnels.arc.nasa.gov

[22] Hollis, B.R., "Real-Gas Flow Properties for NASA Langley Research Center Aerothermodynamic Facilities Complex Wind Tunnels," NASA CR-4755, 1996.